Reactive mass transfer around isolated bubbles rising in a thin-gap cell

Larissa Laurini, Arthur Béteille, Gerhard Fink, Sonja Herres-Pawlis, Karine Loubière

Reactive mass transfer around isolated bubbles rising in a thin-gap cell

Larissa Laurini[1], Arthur Béteille[2], Dr. Gerhard Fink[1], Prof. Dr. Sonja Herres-Pawlis[1], Dr. Karine Loubière[2,3*]

[1] RWTH Aachen University, Institute of Inorganic Chemistry, Landoltweg 1a, 52074 Aachen, Germany

[2] Laboratoire de Génie Chimique, Université de Toulouse, CNRS, INPT, UPS, 4 allée Emile Monso, CS 84234, 31 432 Toulouse cedex 4, France.

[3] Fédération de Recherche FERMAT, CNRS, 135 Av. de Rangueil, 31400 Toulouse, France.

* Email corresponding author: karine.loubiere@cnrs.fr

Abstract

This study investigates reactive mass transfer around isolated bubbles of pure oxygen rising in a thin-gap cell filled with acetonitrile at rest. A colorimetric technique based on the bio-inspired copper(I) complex [Cu(TMG$_2$tol)]OTf is used. The gap- and time-averaged dissolved oxygen concentration fields can be measured in the far-wake of the bubbles with $3 < d < 47$ mm. The variations of the Sherwood numbers with the Peclet numbers show that the mass transfer results obtained are identical with the ones measured earlier with the copper(I) complex [Cu(btmgp)I]. This demonstrates the independency of mass transfer from the properties of the chemical system used. The results significantly enlarge the existing database, which is of great importance to establish robust scaling laws.

Keywords:

Bioinspired copper complex. Bisguanidine ligand. Oxygen bubbles. Reactive mass transfer. Thin-gap cell.

1 Introduction

Many industrial syntheses of bulk chemicals involve reactive bubbly flows in which a gaseous reactant is transferred through a fluidic interface. After mixing with the continuous phase, the gas bubbles are reacting with the dissolved species [1]. Classical examples are hydrogenation, (photo)oxidation, alkylation, polymerization or chlorination [2]. Yield and selectivity of such multiphasic reactions are strongly dependent on the phases' transport phenomena: in fast and competitive reactions the fluid dynamic in the vicinity of the bubbles plays a determining role [3–5]. By understanding the reactive mass transfer mechanisms, the formation of undesired byproducts can be reduced circumventing downstream separation processes and achieving a sustainable upscaling process.

During the last decades, special attention has been paid to the development of cutting-edge technologies for process intensification involving confined geometries such as microreactors, heat-exchanger reactors or monolith reactors [6]. Their characteristic dimensions of micro- or millimetric scale allow efficient mixing, high interfacial areas as well as enhanced heat and mass transfer, making them particularly suitable for improving yield and selectivity of multiphase reactions [7]. In this context, thin-gap flat bubble columns represent an alternative confined geometry, less explored in literature. Therein the bubbles, surrounded by thin lubrication films, rise in a liquid at rest located between two vertical planar plates. With a gap size smaller than the bubble's diameter, the plane geometry enhances mass transfer compared to 3D bubble columns [8]. The in-plane bubble-induced agitation results in an efficient mixing within the liquid phase highly favoring the oxygen transport [9–12]. In addition, the small thickness of the reaction medium faces light attenuation issues, thus making them a promising

application for solar photochemical as well [13–15]. Lastly, thin-gap cells are of great interest for fundamental mass transfer studies as they (i) enable to explore intermediary configurations between fully three-dimensional bubbles and Taylor bubbles and (ii) cover a wide range of motion as well as mass transfer regimes at high Reynolds numbers. While isolated bubbles rising in non-confined liquids have been extensively investigated since 1960 [3,16], the number of works with 2D thin-gap cells remains limited: most of them focuses on hydrodynamics [17–23] and only a few have sudied mass transfer [8,24].

Nowadays, different experimental methods are available to investigate (reactive) interfacial mass transfer at local scale by giving access to the dissolved gas concentration fields. The most frequently used one is Planar Laser-Induced Fluorescence with Inhibition (PLIF-I) [8,25–29] which is applied in various gas-liquid systems including confined interfaces [8, 31]. In PLIF-I, a fluorescent dye is excited with a specific wavelength. Due to different inhibiting factors, like dissolved molecular oxygen, the light emitted undergoes a wavelength shift which can be detected [25,30].

Colorimetric techniques constitute relevant alternatives to PLIF-I as they do not require the use of lasers. Difficulties like matching the excitation wavelength or reflection of fluorescent light from the walls and the bubbles interfaces are thus avoided [31]. Colorimetric techniques involve a reaction between a colorless, diluted molecule and a gaseous species forming a colored product. From the color signal observed in the bubble's wake and vicinity, equivalent dissolved gas concentration fields can be deduced by implementing ad hoc image processing. This was firstly demonstrated by Dietrich et al. [32] with the resazurin dye for Taylor bubbles flowing in a millimetric channel. Later extensions to other confined geometries [33–37] or dyes such as the leuco-indigo carmine followed [38]. The conversion of dyes like leuco-indigo carmine, resazurin or methylene blue with molecular oxygen results in a specific color change with literature-known absorption maxima [39]. However, the use of these dyes for mass transfer investigations is limited since their substrate-specific properties cannot be changed. To create tunable colorimetric reaction systems, coordination chemistry has opened new opportunities in the recent years. Functional groups like amines or aromatic units are combined with transition metals like copper or iron to create molecules which show a strong color change during the conversion with molecular oxygen. Hereby, oxygen functions as an oxidant increasing the oxidation state of the metal atom and thereby changing the electronical structure of the molecule. As a result, the absorption wavelength is being shifted, leading to a strong color change [3,40].

Industrial oxidation processes are using transition metal catalysts with oxygen as oxidant for over 50 years now, but most of them containing harmful and environmentally hazardous elements like chromium, cobalt or nickel [41]. In nature, processes like activation, transfer or reversible binding of oxygen are catalyzed by enzymes [42]. A popular example is the copper enzyme tyrosinase which catalyzes crucial oxidation steps in the formation of the skin and cell pigment melanin [43]. The chemical structure of those enzymes consists of an iron or copper metal center stabilized by amino acids with N-donor ligands like histidine [44–46]. In contrast to complexes with chromium, nickel or cobalt, enzymes are meeting many goals of "green" chemistry: they are not harmful, bio-based and operate under ambient reaction conditions mostly in water [47]. Nevertheless, their industrial field of application is limited since most enzymes' activity is substrate specific, generating only a specific product molecule [48]. An exception displays the enzyme tyrosinase, which is capable to transform either phenols or catechols to quinone products [49]. Hence, coordination chemistry methods are required to mimic this unusual natural substrate diversity and broad the product spectrum while using environmentally-friendly and bio-based elements.

The first catalytically active tyrosinase model system was published only in the last decade. The so called peroxido complex is mimicking the catalytically active Cu_2O_2 center of tyrosinase [49]. Since then several peroxido and oxido catalysts complexes were published converting various simple phenolic substrates [50–54]. Those two Cu_2O_2 species are structural isomers existing in an equilibrium. They can be

transferred into each other by the choice of the ligand system, solvents or coordinating anions [55,56]. Consequently, molecule-specific properties like solubility, physical properties and molecule structure as well as the diffusion coefficient of the reaction system, absorption wavelength or the reaction velocity can be modified. As an example, the copper(I) complexes [Cu(TMGbenza)I] and [Cu(TMGbenza)]OTf, formed by the TMGbenza system, seem to be identical except for the corresponding anion. Nevertheless, their reaction velocity and reaction properties are totally different. The oxido complex generated by [Cu(TMGbenza)I] is stable at room temperature but the formation takes very long (2 h), whereas the one of [Cu(TMGbenza)]OTf is only formed at low temperatures but within 3 minutes [53,54]. As a result, even small modifications on the molecule structure, as the exchange of the corresponding anion, can cause completely different reaction velocities.

In our previous work [24], the bio-inspired copper(I) complex [Cu(btmgp)I] was successfully implemented to unravel the mass transfer around single bubbles freely rising in a thin-gap cell. The chemical reaction used was irreversible and highly sensitive towards oxygen. Hence, a specific experimental set-up was built to operate under oxygen-free conditions with acetonitrile as solvent.

In the present study, two major objectives will be tackled:

- Colorimetric techniques based on bio-inspired copper complexes shall be proven as a generic tool for reactive mass transfer investigations at a local scale.
- The experimental database of mass transfer around single bubbles rising in a thin-gap cell will be enlarged to establish consistent scaling laws.

For this purpose, an optimized copper complex structurally inspired by the last one will be used possessing a different molecule structure, molecular properties and reaction kinetics. [Cu(TMG_2tol)]OTf firstly synthesized by Herres-Pawlis et al. [57] shall prove the independency of the mass transfer from the chemical reaction system. The experiments will be performed in the set-up built in our previous study to enhance comparability [24]. Acetonitrile, a solvent close to industrial conditions, will be used to generate experimental data complementary to the ones of Roig et al. in water [8,19]. The protocol correlating the grey-levels from the colored signal to the equivalent oxygen concentrations will be adapted to account for the features of the new copper complex.

2 Materials and experimental methods

The chemical system, [Cu(TMG_2tol)]OTf, used in this work is highly sensitive towards oxygen, thus working in an inert gas atmosphere was mandatory. Detailed information about the complex preparation, the calibration measurements as well as physical constants and estimations made regarding to the calculation of parameters are given in section S1 in the supporting information.

The molecule structure of the copper(I) complex, [Cu(TMG_2tol)]OTf, used in this study is inspired by the structure of the [Cu(btmgp)I] system determined in 2019 [24]. Both systems consist of two guanidine units bridged by a hydrocarbon backbone. While the btmgp system has a simple propylene backbone, in the TMG_2tol system the two guanidine units are connected by a bulky toluenyl unit (Fig. 1, marked in red). Additionally, the btmgp system contains an iodide anion coordinated to the copper center whereas the triflate anion in the TMG_2tol system is only weakly coordinating and a solvent molecule is connected to the metal center instead (Fig. 1, marked in blue) [24,58]. Due to the high electron density in the aromatic toluene backbone, the TMG_2tol system is strongly fluorescent. Hence, it is not limited to investigations in the UV/Vis area with colorimetric methods; unlike the btmgp system, the TMG_2tol system could be suitable for fluorescence studies as well [3].

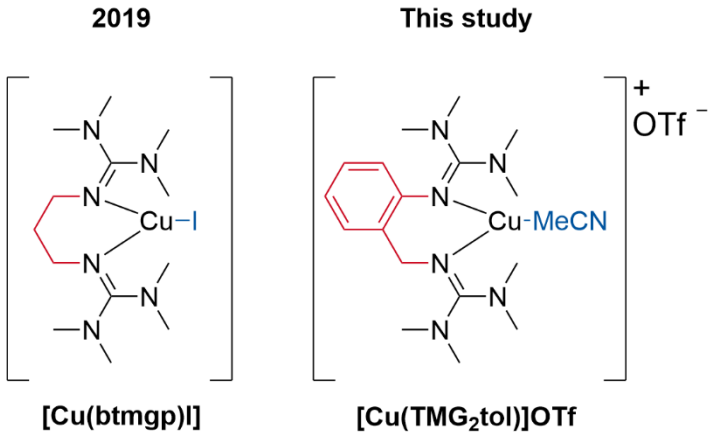

Figure 1. Comparison of the molecule structures of [Cu(btmgp)I] studied in 2019 [24] and [Cu(TMG$_2$tol)]OTf investigated in this study (MeCN = CH_3CN = acetonitrile).

As with the btmgp system used in 2019 [24], the colorless copper (I) complex [Cu(TMG$_2$tol)]OTf is oxidized to an orange Cu(III) oxido complex when converted with molecular oxygen. As the orange copper(III) complex is not stable at ambient temperatures, a consecutive decay reaction to a stable green copper(II) complex takes place. In contrast to the btmgp system, which generates a mixture of two green permanent reaction products, only one green copper (II) product is obtained in this case (Fig. 2). A detailed description of the kinetics can be found in section 3.2.

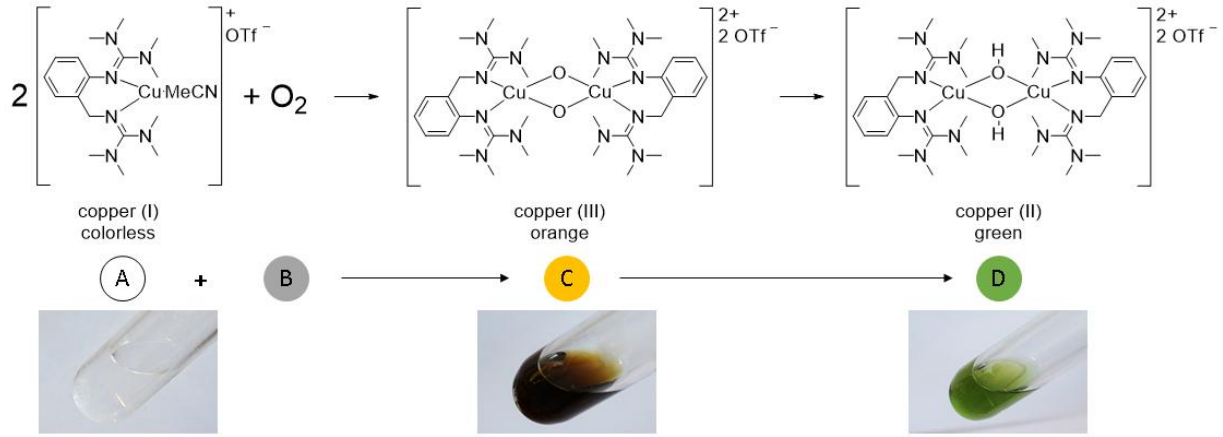

Figure 2. Oxidation of the colorless copper(I) complex [Cu(TMG$_2$tol)]OTf to the unstable, orange colored copper(III) complex and consecutive decay reaction to the stable, green colored copper(II) complex. (OTf = CF_3SO_3; MeCN = CH_3CN).

The experimental set-up, the imaging system and the image processing were almost identical to the one used in 2019 [24]. They are depicted in detail in section S1 in the supporting information.

3 Results and discussion

3.1 Bubble kinematics

In this work, 38 isolated oxygen bubbles were generated in the thin-gap cell (see Table S2 in the supporting information). Their in-plane equivalent diameters d (defined in Eq. S1 in the supporting information) are larger than the gap width (h=1.062 ± 0.005 mm) ranging from 3 mm to 47 mm. Their in-

plane motion was characterized by mean bubble velocities, V_b, varied between 0.12 and 0.21 m s^{-1} (V_b was defined as the time-averaged vertical component of the bubble velocity, $\langle V_x \rangle$). The bubble Reynolds numbers, $Re = \frac{\rho_L V_b d}{\mu_L}$, ranged from 1200 to 15000, the Archimedes numbers, $Ar = \frac{\rho_L \sqrt{gd} d}{\mu_L}$, from 2100 to 34000 and the Bond numbers, $Bo = \frac{\rho_L g d^2}{\sigma_L}$, from 6 to 240. It can be noticed that these dimensionless numbers cover a wider range than in our previous work [24].

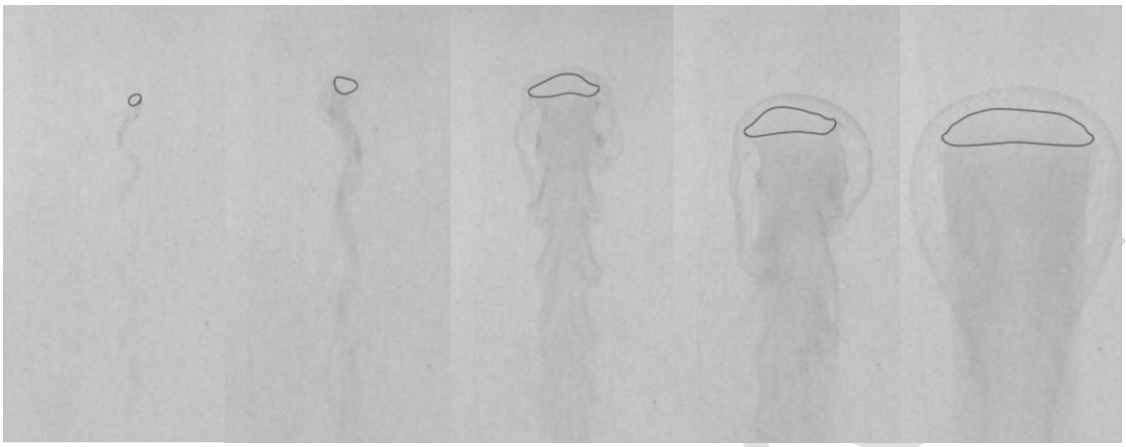

Figure 3: Raw images of the visible reactive color signal in the bubble's wake of different sizes obtained in the present study with the [Cu(TMG$_2$tol)]OTf complex. No red band-pass filter was used here.

The flattened bubbles are followed by contrasted regimes of oscillatory motions as illustrated in Fig. 3 (five examples of raw data are given in the supporting information as download). Thereby, the colored temporal signals visualize the oxygen transport from the gas bubble into the liquid phase and work as an indirect measure for the fluctuation of the velocity field in the bubbles wake and vicinity. As observed with the btmgp copper complex [24], for small bubbles, the path is unsteady and oxygen is collected by the released vortices. With increasing bubble size, shape oscillations start to appear superposing the path oscillation and tuning the unsteady wake. Reaching large bubble sizes, the previously unsteady wake stabilizes completely by taking a large strip shape while a halo can be observed in front of the bubble.

Fig. 4 and Fig.5 display the variation of the bubble Reynolds number, *Re*, as a function of the Archimedes number, *Ar*, and the variation of the bubble aspect ratio, χ, as a function of the Weber number, $We = \frac{\rho_L V_b^2 d}{\sigma_L}$. As the bubble's diameter, shape and velocity change with the rising bubble, these dimensionless numbers are actually time-dependent. Thus, mean values were used for plotting these figures. The data obtained are compared with the btmgp complex used under the same reaction conditions (*h*= 1 mm) and the ones of Roig et al. (2015) (*h*= 3 mm) [19] as well as Roig et al. (2017) (*h*= 1 mm) [8] measured in water.

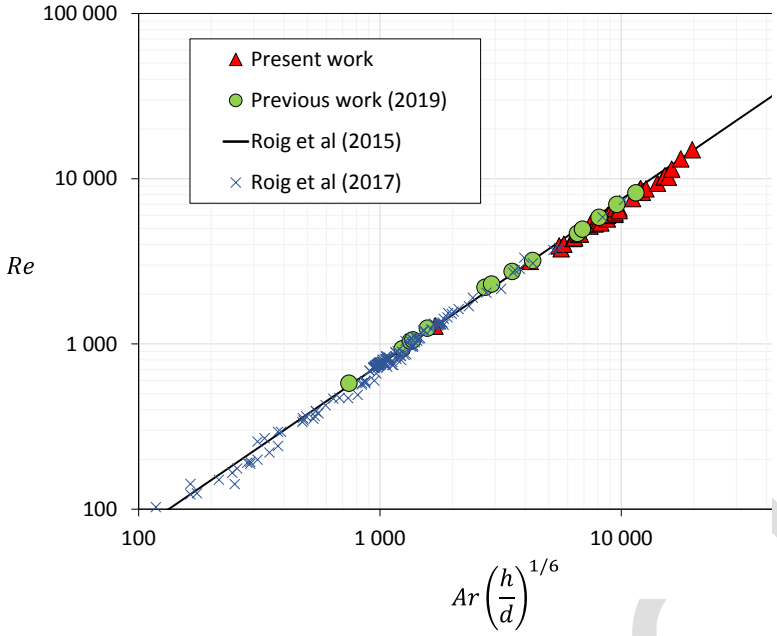

Figure 4: Variation of the bubble Reynolds number as a function of the modified Archimedes number.

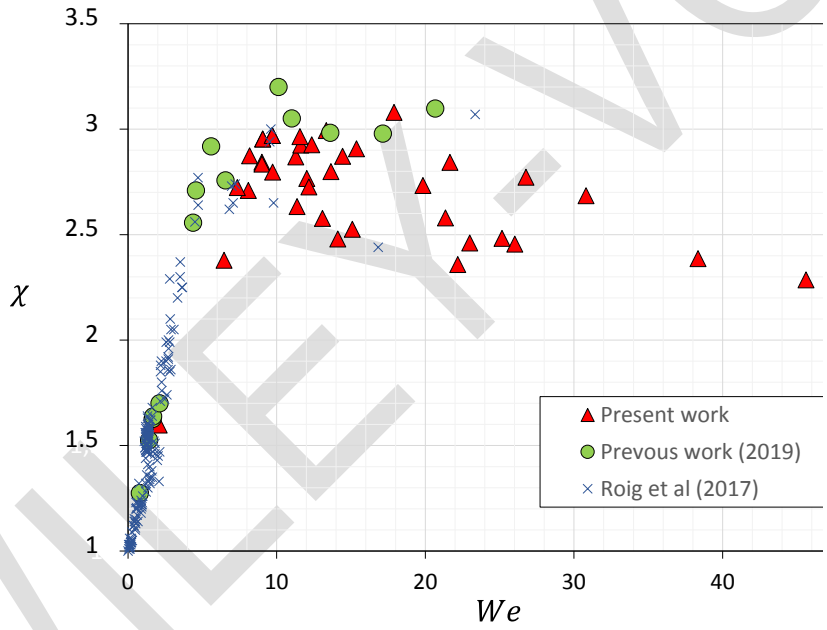

Figure 5 : Variation of the aspect ratio as a function of the Weber number.

The scaling law (1) proposed by Roig et al. in 2015 can predict all experimental Reynolds numbers proving the presence of similar inertial regimes independent from the gap width *h* and the liquid phase (see Fig. 4). Hence, any drag force is exerted by the liquid films.

$$Re = 0.75Ar\left(\frac{h}{d}\right)^{1/6} \quad (1)$$

In accordance to our previous work [24], bubbles with identical diameters are more flattened than in water due to the lower surface tension (σ_L = 28.7 mN m^{-1}) and viscosity (μ_L = 0.369 mPa s) of acetonitrile. The aspect ratio ranges from 1.6 to 3.1 showing a significant dispersion around asymptotic maximum values (> 2.5). It varies with the Weber number analogous to the other studies. However, with the present TMG_2tol complex higher Weber numbers (We = 45) are achieved than with the previous btmgp complex (We = 20). These deviations could be originated from the strong shape oscillations of

the bubbles occurring in acetonitrile. In contrast, in water bubbles with stationary, hemi cylindrical shapes were observed. [8,19].

3.2 Decay of the intermediary orange Cu(III) complex and calibration procedure

As with the btmgp system used in 2019 [24], the colorless TMG_2tol complex reacts with molecular oxygen to form an orange Cu(III) oxido complex that is not stable at ambient temperature and thus decays into a stable green copper(II) complex (see Fig. 2). The pictures reported in Fig. 3, acquired without red band-pass filter, are an easy way to visualize this decay. The colored signal is clearly distinguishable in the near-field wake of the bubble. But, after a certain axial distance after the bubble, this signal is increasingly attenuating until it becomes entirely invisible when the conversion of the Cu(III) complex into the Cu(II) complex is complete. By implementing a specific algorithm on Matlab® software, it was possible to extract the variations of the grey-level (GV) value intensity along a line in the wake of the bubble, as detailed in section S2.2 in the supporting information. By processing the decay curves behind almost 30 bubbles, a mean value of the decay factor β equal to 4.5 s^{-1} was obtained. In comparison with the btmgp complex for which β =2.5 s^{-1}, the vanishing rate of the TMG_2tol complex is almost two times faster [24]. This result is in good agreement with data from stopped-flow measurements indicating a 1.5 times faster decay for [Cu(TMG_2tol)]OTf (1.8 ±0.3 s^{-1}) [57] than for [Cu(btmgp)I] (1.27 ±0.03 s^{-1}) [59]. Due to the fast decay, the formation rate for the orange copper(III) complex could only be quantified at temperatures below – 50°C by stopped-flow measurements (as explained in section 3.3). Therefore, the orange copper(III) complex was considered not to be stable at room temperature [57]. Nevertheless – and rather unexpected-, the orange color was visible for a short amount of time during bubble acquisition at room temperature (videos can be found and downloaded under: https://doi.org/10.5446/60173 (in real speed) and https://doi.org/10.5446/60174 (in slow motion)).

Such fast decay has a direct consequence for implementing the calibration procedure linking the GV intensity to the "equivalent" dissolved oxygen concentration, as done in the resazurin-based colorimetric methods [32,34,35]. As the orange signal can only be captured in the vicinity and in the near-field wake of the bubble (see Fig. 3), the calibration under this color signal is not possible. However, as the kinetics of the decay reaction is very fast (4.5 s^{-1}), one can assume that in the far-field wake of the bubble, the wholeness of the colored signal is originated from the final green product. For this reason, as in our previous work [24], the calibration curve will consider the green signal of the Cu(II) complex. In contrast to the former study, a red band-pass filter (see section S1.5 in the supporting information) has been used to increase the contrast ratio of the grey-levels seen by the camera when the final pale-green signal was present in the far-field wake. The experimental protocol for establishing the calibration curve was identical to the one used in 2019 [24] (see sections S1.2 and S2.3 in the supporting information).

3.3 Mass flux and Sherwood number

Fig. 3 illustrates the strong dependency of the oxygen deposit on the bubble size. As first described by Roig et al. [8], the amount as well as the complicated topology of the oxygen deposit result from the interfacial mass transfer taking place in the thin liquid films and the high Reynolds number in-plane flow of the bubble's vicinity. For larger diameters, a layer of high GV values increasing with the bubble size can be observed in front of the bubbles. These halos might originate from vortices produced by the bubbles' confinement [8]. Subsequently, the oxygen transferred at this peripheral interfacial region is transported by the flow all around and past the bubble. It is later recombined with the amount transferred at the liquid films between the bubble and the walls of the cell [24]. The related oxygen concentration cannot be quantified due to the fast decay of the orange complex. Furthermore,

identifying the contribution of each mass transfer mechanism is not possible without any information about the flow dynamics.

By applying the calibration relationship (Eq. S4 in the supporting information) to the effective absorption signal extracted from the images acquired with the red band-width filter, the equivalent gap- and time-averaged oxygen concentration fields can be deduced in the far-field wake of the bubble. Then, the same procedure as used before was applied to calculate the Sherwood number from these concentration fields [24]. Note that in the supporting information, the main steps of this procedure are reminded (section S2.4) and Table S.2 lists the in-plane diameter, the aspect ratio, the velocity, the areas of the peripheral interface in contact with the in-plane flow and on the liquid films, in addition to the Reynolds, Weber, Bond, Sherwood as well as Peclet numbers for each bubble.

Fig. 6 reports the variation of the Sherwood number, $Sh = \frac{\langle \varphi \rangle \, d}{\mathfrak{D}_{O_2} C^*_{O_2}}$, as a function of the Peclet number, $Pe = \frac{V_b \, d}{\mathfrak{D}_{O_2}}$. Experimental data from the present study with the TMG_2tol complex (*h*= 1 mm) and the previous one with the btmgp complex (*h*= 1 mm) [24] in acetonitrile as well as experimental data from Roig et al. [8] obtained in water (*h*= 1 mm) are compared. Additionally, the values given by the scaling law model (Equation 2) of Roig et al. [8] are displayed.

$$Sh = 1.126 \, Pe^{0.5} \tag{2}$$

As expected, Peclet number and mass transfer increase in parallel. For a given Peclet number, identical Sherwood numbers are obtained, no matter if the TMG_2tol or the btmgp copper complex is used. Thus, the mass transfer of oxygen from the bubble into the liquid phase is independent from the chemical system used.

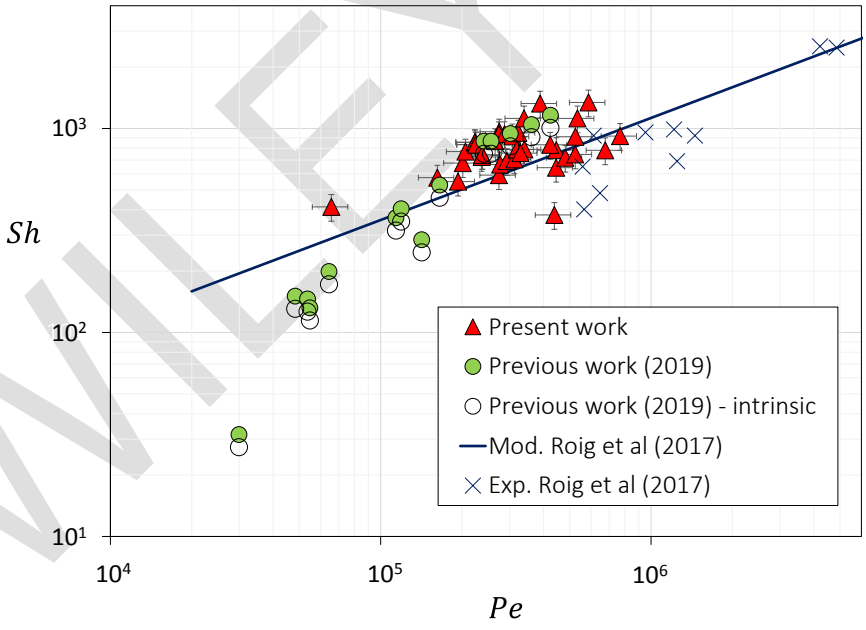

Figure 6: Variation of the Sherwood number as a function of the Peclet number. In comparison, the experimental data of our previous study (2019) (*h*= 1 mm) [24]obtained with the btmgp complex in acetonitrile and the ones of Roig et al. (2017) (h= 1 mm) [8] obtained in water are reported. Empty circles correspond to Sherwood numbers corrected by enhancement factors.

In our previous paper [24], the Hatta number, *Ha*, and the enhancement factor, *E*, were calculated to evaluate a possible enhancement of the mass transfer by the reaction. With the present TMG_2tol

complex such calculation could not be performed. It was not possible to measure the kinetic constant of the formation of the orange copper(III) complex, *k*, in the stopped-flow set-up, as done by [24] with the btmgp copper complex. Indeed, at room temperature, formation and decay of the orange species are competing with one another while they can be decorrelated at low temperatures [57]. In the stopped-flow set-up, the procedure used to study the oxygenation kinetics involves an oxygen saturated solution, inducing high oxygen concentration in the entire measuring volume. Consequently, formation and decay taking place at the same time and a complete formation before the complex already starts to decay cannot be observed. In the Hele-Shaw cell, the situation is different as the single bubbles of pure oxygen are rising in an oxygen-free reaction solution: strong gradients of oxygen concentration are existing in the vicinity of the bubble. Those are due to three-dimensional flows resulting from the vortices produced by the confinement of the bubble [24]. These gradients locally slow down the oxygenation reaction and thus enable the detection of the orange species before its decay, which was not expected initially.

Despite the fact that the kinetic constant of the formation of the orange complex, *k*, is unknown, one can assume that *k* is a priori higher than the one in the btmgp complex (*k* =3707±500 L mol^{-1} s^{-1}, see [24]). Knowing that the diffusion coefficient of the present copper complex is slightly higher (+10%) than the one of the btmgp complex (see section S1.1 in the supporting information), for the same measured Sherwood number, a faster formation of the orange complex would induce a higher Hatta number, which definition for a second-order reaction is recalled below [60] by

$$Ha = \frac{\sqrt{kC_{Cu}\mathcal{D}_{O_2}}}{k_L} \quad (3)$$

Where k_L is the liquid-side mass transfer coefficient.

By this way, the enhancement factor with the present TMG_2tol complex can be estimated to be higher or at least equal to the one with the btmgp complex (i.e. *E* < 1.12-1.15).

Another interesting fact is that the Sherwood numbers measured with both copper complexes in acetonitrile cannot be predicted by the scaling law (Eq. 2) proposed by [8] in water, in particular when the Peclet numbers fall down below 10^5. This expected result can be explained by several reasons: (i) the effect of surface tension is not considered in this law (σ_L = 28.4 mN m^{-1} in acetonitrile and σ_L = 72.0 mN m^{-1} in water (25°C) [61]), and (ii) the Schmidt number, *Sc*, varies from 51 in acetonitrile to 348 in water. In addition, this scaling law was established considering only large bubbles. The case of small bubbles could not be investigated by [8] using the PLIF-I technique. However, as shown in Fig. 3, bubble dynamics and mass transfer are highly depending on the bubble's diameter. Especially the vortices periodically released in the wake playing a significant role. Thus, contributions to the overall mass transfer occurring in the peripheral interfacial region of the bubble as well as in the thin films at the walls are strongly influenced by the bubble diameter. This could lead to Peclet numbers with an exponent different of 0.5.

The present study enlarges the database of mass transfer investigations in thin-gap cells using an optimized copper complex in acetonitrile. A wide range of dimensionless numbers (Re, We and Ar) twice as large as with the former btmgp complex is covered. Some of the scaling laws proposed by Roig et al. [8] cannot be transferred to the present data as these laws are based on water only considering large bubble diameters. To adapt the existing scaling laws as well as propose new ones, further data with a variation of surface tension, gap-wide and bubble diameter are needed. Thereby, colorimetric techniques and a chemical system operating in other solvents than water or acetonitrile should be used focusing on smaller bubble diameters as those cannot be cover with PLIF-I technique.

4 Conclusion

This study demonstrated the independence of the mass transfer of oxygen between a gas bubble and a liquid phase from the structure, properties and reaction kinetics of the copper complex molecules used. Hence, bio-inspired copper(I) complexes are proven as a powerful tool to investigate reactive mass transfer in bubbly flows at the local using organic solvents close to the industrial conditions. In addition, this work contributes to enlarge the existing experimental database related to the dynamics and mass transfer of single bubbles rising in a thin-gap cell. However, new experiments with copper complexes using colorimetric techniques with other solvents than acetonitrile and water are required focusing on small bubble diameters to revise the existing scaling laws. In particular, by introducing the Schmidt numbers ($Pe = Re \times Sc$) and/or the Morton number ($Mo = \frac{g\,\mu_L^4}{\rho_L \sigma_L^3}$), Sherwood numbers for Peclet numbers varying from 10^4 to 10^7 could be predicted.

Supporting Information

Supporting Information for this article can be found under [Link provided by Wiley].

Acknowledgment

The authors wish to acknowledge Alain Pontier for his technical support, Emmanuel Cid for his help concerning the image acquisition and Francisco Felis for his guidance on the image post-processing. Further we thank Markus Reichelt and the DWI Aachen for measuring the surface tension and providing their tensiometer. Also, the authors thank the laboratory LCC (CNRS UPR 8241) at the ENSIACET in Toulouse for providing their glovebox. The authors acknowledge RADAR4Chem and the technical information library (TIB) Hannover for the support and the funding of their repositories. Lastly, the authors are grateful for the short-time fellowship given to Larissa Laurini from the German Academic Exchange Service (DAAD) to financially support her research stay at the LGC lab in Toulouse.

Symbols

A	[-]	window-averaged absorption signal, dimensionless (defined in Eq. S3 in the supporting information)
C	[mol L^{-1}]	concentration
d	[m]	in-plane equivalent bubble diameter (defined in Eq. S1 in the supporting information)
$\mathfrak{D}$	[m^2 s^{-1}]	diffusion coefficient
g	[m s^{-2}]	gravity constant
h	[m]	gap width
h_f	[m]	lubrification film thickness (section S2.4 in the supporting information)
I	[-]	grey-level volume intensity, dimensionless (section S2.3 in the supporting information)
k	[L mol^{-1} s^{-1}]	kinetic formation constant of the copper complex
k_L	[m s^{-1}]	liquid-side mass transfer coefficient
m	[kg]	mass of oxygen deposited (defined in Eq. S5 in the supporting information)
M	[g mol^{-1}]	molar mass (section S1.2 in the supporting information)
P	[m]	perimeter of projected surface (section S1.5 in the supporting information)
S	[m²]	bubble in-plane projected area
S_p	[m²]	area of the peripheral interface in contact with the in-plane flow (Fig. S2 in the supporting information)
S_f	[m²]	areas of the liquid film (Fig. S2 in the supporting information)
t	[s]	time
V	[L]	volume (section S1.2 in the supporting information)
V_b	[m s^{-1}]	mean bubble velocity (defined in section S1.5 in the supporting information)
V_x	[m s^{-1}]	bubble velocity

Greek letters

β	[s^{-1}]	decay factor
μ_L	[Pa s]	liquid dynamic viscosity
ν_L	[m^2 s^{-1}]	liquid kinematic viscosity (section S2.3 in the supporting information)
ρ_L	[kg m^{-3}]	liquid density
σ_L	[N m^{-1}]	surface tension
Φ	[kg s^{-1}]	mass flux of oxygen transferred (defined in Eq. S6 in the supporting information)
φ	[kg m^{-2} s^{-1}]	mass flux density of oxygen transferred (defined in Eq. S7 in the supporting information)
χ	[-]	bubble aspect ratio, dimensionless

Dimensionless numbers

Ar	Archimedes number
Bo	Bond number
E	Enhancement factor
Ha	Hatta number
Mo	Morton number
Pe	Peclet number
Re	Reynolds number
Sc	Schmidt number
Sh	Sherwood number
We	Weber number

Subscripts

b	bubble
Cu	copper complex
O_2	oxygen
W	water

Abbreviations

GV	grey-level
MeCN	acetonitrile (CH_3CN)
OD	optical density
OTf	triflate (CF_3SO_3)
PLIF-I	Planar Laser-Induced Fluorescence with Inhibition
ROI	region-of-interest

References

[1] W. D. Deckwer, R. W. Field, *Bubble Column Reactors*, Wiley, Chichester, NY, USA **1992.**

[2] N. Kantarci, F. Borak, K. O. Ulgen, *Process Biochem.* **2005**, *40 (7)*, 2263–2283. DOI: 10.1016/j.procbio.2004.10.004

[3] M. Schlüter, D. Bothe, S. Herres-Pawlis, U. Nieken, *Reactive Bubbly Flows*, Springer International Publishing, Cham, Germany **2021.**

[4] P. Rollbusch, M. Bothe, M. Becker, M. Ludwig, M. Grünewald, M. Schlüter, R. Franke, *Chem. Eng. Sci.* **2015**, *126*, 660–678. DOI: 10.1016/j.ces.2014.11.061

[5] M. Schlüter, S. Herres-Pawlis, U. Nieken, U. Tuttlies, D. Bothe, *Annu. Rev. Chem. Biomol. Eng.* **2021**, *12*, 625–643. DOI: 10.1146/annurev-chembioeng-092220-100517

[6] A. I. Stankiewicz, T. van Gerven, G. Stefanidis, *The fundamentals of process intensification*, Wiley-VCH, Weinheim, Germany **2019.**

[7] M. N. Kashid, L. Kiwi-Minsker, *Ind. Eng. Chem. Res.* **2009**, *48 (14)*, 6465–6485. DOI: 10.1021/ie8017912

[8] M. Roudet, A.-M. Billet, S. Cazin, F. Risso, V. Roig, *AIChE J.* **2017**, *63 (6)*, 2394–2408. DOI: 10.1002/aic.15562

[9] E. Bouche, V. Roig, F. Risso, A.-M. Billet, *J. Fluid Mech.* **2012**, *704*, 211–231. DOI: 10.1017/jfm.2012.233

[10] E. Bouche, V. Roig, F. Risso, A.-M. Billet, *J. Fluid Mech.* **2014**, *758*, 508–521. DOI: 10.1017/jfm.2014.544

[11] E. Alméras, S. Cazin, V. Roig, F. Risso, F. Augier, C. Plais, *Int. J. Multiphase Flow* **2016**, *83*, 153–161. DOI: 10.1016/j.ijmultiphaseflow.2016.03.011

[12] E. Alméras, F. Risso, V. Roig, C. Plais, F. Augier, *Phys. Rev. Fluids* **2018**, *3 (7)*, 1–19. DOI: 10.1103/PhysRevFluids.3.074307

[13] D. Bahnemann, *Sol. Energy* **2004**, *77 (5)*, 445–459. DOI: 10.1016/j.solener.2004.03.031

[14] C. Thobie, E. Gadoin, W. Blel, J. Pruvost, C. Gentric, *Chem. Eng. Process.* **2017**, *122*, 76–89. DOI: 10.1016/j.cep.2017.10.009

[15] M. Oelgemöller, *Chem. Rev.* **2016**, *116 (17)*, 9664–9682. DOI: 10.1021/acs.chemrev.5b00720

[16] R. M. Griffith, *Chem. Eng. Sci.* **1960**, *12 (3)*, 198–213. DOI: 10.1016/0009-2509(60)85006-3

[17] Figueroa-Espinoza B., R. Zenit, D. Legendre, *J. Fluid Mech.* **2008**, *616*, 419–443. DOI: 10.1017/S0022112008004072

[18] V. Roig, M. Roudet, F. Risso, A.-M. Billet, *J. Fluid Mech.* **2012**, *707*, 444–466. DOI: 10.1017/jfm.2012.289

[19] A. Filella, P. Ern, V. Roig, *J. Fluid Mech.* **2015**, *778*, 60–88. DOI: 10.1017/jfm.2015.355

[20] M. Hashida, K. Hayashi, A. Tomiyama, *Int. J. Multiphase Flow* **2019**, *111*, 285–293. DOI: 10.1016/j.ijmultiphaseflow.2018.09.015

[21] M. Gumulya, R. P. Utikar, V. K. Pareek, G. M. Evans, J. B. Joshi, *Chem. Eng. J.* **2021**, *405*, 1–20. DOI: 10.1016/j.cej.2020.126615

[22] L. Böhm, M. Brehmer, M. Kraume, *Chem. Ing. Tech.* **2016**, *88 (1-2)*, 93–106. DOI: 10.1002/cite.201500105

[23] S. Almani, W. Blel, E. Gadoin, C. Gentric, *Chem. Eng. Res. Des.* **2021**, *167*, 218–230. DOI: 10.1016/j.cherd.2021.01.010

[24] F. Felis, F. Strassl, L. Laurini, N. Dietrich, A.-M. Billet, V. Roig, S. Herres-Pawlis, K. Loubière, *Chem. Eng. Sci.* **2019**, *207*, 1256–1269. DOI: 10.1016/j.ces.2019.07.045

[25] S. Rüttinger, C. Spille, M. Hoffmann, M. Schlüter, *ChemBioEng Rev.* **2018**, *5 (4)*, 253–269. DOI: 10.1002/cben.201800005

[26] G. Lebrun, F. Xu, C. Le Men, G. Hébrard, N. Dietrich, *Fluids* **2021**, *6 (2)*, 84–99. DOI: 10.3390/fluids6020084

[27] M. Jimenez, N. Dietrich, G. Hébrard, *Chem. Eng. Sci.* **2013**, *100*, 160–171. DOI: 10.1016/j.ces.2013.01.036
[28] A. Weiner, J. Timmermann, C. Pesci, J. Grewe, M. Hoffmann, M. Schlüter, D. Bothe, *Chem. Eng. Sci.: X* **2019**, *1*, 1–18. DOI: 10.1016/j.cesx.2019.100007
[29] U. D. Kück, M. Schlüter, N. Räbiger, *J. Chem. Eng. Jpn.* **2012**, *45 (9)*, 708–712. DOI: 10.1252/jcej.12we059
[30] A. Dani, P. Guiraud, A. Cockx, *Chem. Eng. Sci.* **2007**, *62 (24)*, 7245–7252. DOI: 10.1016/j.ces.2007.08.047
[31] C. Butler, B. Lalanne, K. Sandmann, E. Cid, A.-M. Billet, *Int. J. Multiphase Flow* **2018**, *105*, 185–201. DOI: 10.1016/j.ijmultiphaseflow.2018.04.005
[32] N. Dietrich, K. Loubière, M. Jimenez, G. Hébrard, C. Gourdon, *Chem. Eng. Sci.* **2013**, *100*, 172–182. DOI: 10.1016/j.ces.2013.03.041
[33] L. Yang, K. Loubière, N. Dietrich, C. Le Men, C. Gourdon, G. Hébrard, *Chem. Eng. Sci.* **2017**, *165*, 192–203. DOI: 10.1016/j.ces.2017.03.007
[34] M. Mei, G. Hébrard, N. Dietrich, K. Loubière, *Chem. Eng. Sci.* **2020**, *222*, 115717. DOI: 10.1016/j.ces.2020.115717
[35] M. Mei, C. Le Men, K. Loubière, G. Hébrard, N. Dietrich, *Chem. Eng. Sci.* **2022**, *258*, 117752. DOI: 10.1016/j.ces.2022.117752
[36] A. Canado, C. Lemen, M. Pages, F. Violleau, N. Dietrich, G. Hébrard, *Int. J. Heat Mass Transfer* **2022**, *189*, 122672. DOI: 10.1016/j.ijheatmasstransfer.2022.122672
[37] P. Kováts, D. Pohl, D. Thévenin, K. Zähringer, *Chem. Eng. Sci.* **2018**, *190*, 273–285. DOI: 10.1016/j.ces.2018.06.029
[38] W. Krieger, M. Hörbelt, S. Schuster, J. Hennekes, N. Kockmann, *Chem. Eng. Technol.* **2019**, *42 (10)*, 2052–2060. DOI: 10.1002/ceat.201800753
[39] P. G. Tratnyek, T. E. Reilkoff, A. W. Lemon, M. M. Scherer, B. A. Balko, L. M. Feik, B. D. Henegar, *Chem. Educ.* **2001**, *6 (3)*, 172–179. DOI: 10.1007/s00897010471a
[40] M. Paul, F. Strassl, A. Hoffmann, M. Hoffmann, M. Schlüter, S. Herres-Pawlis, *Eur. J. Inorg. Chem.* **2018**, *2018 (20-21)*, 2101–2124. DOI: 10.1002/ejic.201800146
[41] F. Cavani, J. H. Teles, *ChemSusChem* **2009**, *2 (6)*, 508–534. DOI: 10.1002/cssc.200900020
[42] A. S. Bommarius, B. Riebel, *Biocatalysis*: *Fundamentals and applications*, Wiley-VCH, Weinheim, Germany **2002.**
[43] J. J. Stephanos, A. W. Addison, *Chemistry of Metalloproteins: Problems and Solutions in Bioinorganic Chemis*, John Wiley & Sons, Hoboken, NJ, USA **2014.**
[44] M. F. PERUTZ, M. G. Rossmann, A. F. Cullis, H. Muirhead, G. Will, A. C. North, *Nature* **1960**, *185 (4711)*, 416–422. DOI: 10.1038/185416a0
[45] J. C. Kendrew, R. E. Dickerson, B. E. Strandberg, R. G. Hart, D. R. Davies, D. C. Phillips, V. C. Shore, *Nature* **1960**, *185 (4711)*, 422–427. DOI: 10.1038/185422a0
[46] Y. Matoba, T. Kumagai, A. Yamamoto, H. Yoshitsu, M. Sugiyama, *J. Biol. Chem.* **2006**, *281 (13)*, 8981–8990. DOI: 10.1074/jbc.M509785200
[47] R. A. Sheldon, D. Brady, *ChemSusChem* **2019**, *12 (13)*, 2859–2881. DOI: 10.1002/cssc.201900351
[48] S. Wu, R. Snajdrova, J. C. Moore, K. Baldenius, U. T. Bornscheuer, *Angew. Chem., Int. Ed.* **2021**, *60 (1)*, 88–119. DOI: 10.1002/anie.202006648
[49] M. Rolff, J. Schottenheim, H. Decker, F. Tuczek, *Chem. Soc. Rev.* **2011**, *40 (7)*, 4077–4098. DOI: 10.1039/c0cs00202j
[50] B. Herzigkeit, B. M. Flöser, N. E. Meißner, T. A. Engesser, F. Tuczek, *ChemCatChem* **2018**, *10 (23)*, 5402–5405. DOI: 10.1002/cctc.201801606
[51] M. S. Askari, K. V. N. Esguerra, J.-P. Lumb, X. Ottenwaelder, *Inorg. Chem.* **2015**, *54 (17)*, 8665–8672. DOI: 10.1021/acs.inorgchem.5b01297

[52] A. Hoffmann, C. Citek, S. Binder, A. Goos, M. Rübhausen, O. Troeppner, I. Ivanović-Burmazović, E. C. Wasinger, T. D. P. Stack, S. Herres-Pawlis, *Angew. Chem., Int. Ed.* **2013**, *52 (20)*, 5398–5401. DOI: 10.1002/anie.201301249

[53] M. Paul, M. Teubner, B. Grimm-Lebsanft, C. Golchert, Y. Meiners, L. Senft, K. Keisers, P. Liebhäuser, T. Rösener, F. Biebl et al., *Chem. - Eur. J.* **2020**, *26 (34)*, 7556–7562. DOI: 10.1002/chem.202000664

[54] M. Paul, A. Hoffmann, S. Herres-Pawlis, *J. Biol. Inorg. Chem.* **2021**, *26 (2-3)*, 249–263. DOI: 10.1007/s00775-021-01849-9

[55] E. A. Lewis, W. B. Tolman, *Chem. Rev.* **2004**, *104 (2)*, 1047–1076. DOI: 10.1021/cr020633r

[56] C. E. Elwell, N. L. Gagnon, B. D. Neisen, D. Dhar, A. D. Spaeth, G. M. Yee, W. B. Tolman, *Chem. Rev.* **2017**, *117 (3)*, 2059–2107. DOI: 10.1021/acs.chemrev.6b00636

[57] F. Strassl, B. Grimm-Lebsanft, D. Rukser, F. Biebl, M. Biednov, C. Brett, R. Timmermann, F. Metz, A. Hoffmann, M. Rübhausen et al., *Eur. J. Inorg. Chem.* **2017**, *2017 (27)*, 3350–3359. DOI: 10.1002/ejic.201700528

[58] S. Herres, A. J. Heuwing, U. Flörke, J. Schneider, G. Henkel, *Inorg. Chim. Acta* **2005**, *358 (4)*, 1089–1095. DOI: 10.1016/j.ica.2004.10.009

[59] D. Schurr, F. Strassl, P. Liebhäuser, G. Rinke, R. Dittmeyer, S. Herres-Pawlis, *React. Chem. Eng.* **2016**, *1 (5)*, 485–493. DOI: 10.1039/C6RE00119J

[60] O. Levenspiel, *Chemical reaction engineering*, 3 ed., Wiley, New York, USA **1999.**

[61] W. M. Haynes, *CRC Handbook of Chemistry and Physics*, 95 ed., CRC Press **2014.**

Table and Figure captions

Figure 1. Comparison of the molecule structures of [Cu(btmgp)I] studied in 2019 [24] and [Cu(TMG_2tol)]OTf investigated in this study (MeCN = CH_3CN = acetonitrile).

Figure 2. Oxidation of the colorless copper(I) complex [Cu(TMG_2tol)]OTf to the unstable, orange colored copper(III) complex and consecutive decay reaction to the stable, green colored copper(II) complex. (OTf = CF_3SO_3; MeCN = CH_3CN).

Figure 3: Raw images of the visible reactive color signal in the bubble's wake of different sizes obtained in the present study with the [Cu(TMG_2tol)]OTf complex. No red band-pass filter was used here.

Figure 4: Variation of the bubble Reynolds number as a function of the modified Archimedes number.

Figure 5: Variation of the aspect ratio as a function of the Weber number.

Figure 6: Variation of the Sherwood number as a function of the Peclet number. In comparison, the experimental data of our previous study (2019) (*h*= 1 mm) [24]obtained with the btmgp complex in acetonitrile and the ones of Roig et al. (2017) (h= 1 mm) [8] obtained in water are reported. Empty circles correspond to Sherwood numbers corrected by enhancement factors.

Entry for the Table of Contents

Type of Article: Research article

Single pure oxygen bubbles are freely rising in a thin-gap cell with colorless copper(I) complex solution at rest. In the bubble's wake and vicinity a fast reaction between the copper(I) complex and oxygen to an unstable orange copper(III) complex occurs which quickly decays into an green copper(II) complex.

Reactive mass transfer around isolated bubbles rising in a thin-gap cell

L. Laurini, A. Béteille, G. Fink, S. Herres-Pawlis, K. Loubière*

Chem. Eng. Technol. **20XX**, *XX (X)*,

xxxx...xxxx